PCCP

Accepted Manuscript

ROYAL SOCIETY OF CHEMISTRY

www.rsc.org/pccp

Journal Name

ARTICLE

High Performance Lithium Storage in Ultrafine Manganese Fluoride Nanorod Anode with Enhanced Electrochemical Activation Process Based on Conversion Reaction

Received 00th January 20xx,
Accepted 00th January 20xx

DOI: 10.1039/x0xx00000x

www.rsc.org/

Kun Rui, [a] Zhaoyin Wen, [*a] Xiao Huang, [a] Yan Lu, [a] Jun Jin [a] and Chen Shen [a]

A facile one-step solvothermal reaction route for preparation of manganese fluoride nanorods is developed successfully using manganese (II) chloride tetrahydrate ($MnCl_2•4H_2O$) as manganese source and ionic liquid 1-Butyl-3-methylimidazolium tetrafluoroborate ($BmimBF_4$) as fluorine source. Measurements including X-ray diffraction, field-emission scanning electron microscopy and high-resolution transmission electron microscopy are conducted to characterize the structural and microstructure properties of the synthesized MnF_2. Pure phase tetragonal MnF_2 displays nanorod-like morphology with a diameter of about 20 nm and length of several hundred nanometers. Electrochemical performance of MnF_2 nanorod anode for rechargeable lithium batteries is investigated. A reversible discharge capacity as high as 443 mAh g^{-1} at 0.1 C is obtained for lithium uptake reaction with an initial discharge plateau around 0.7 V. The striking enhancement in electrochemical Li storage performance in ultrafine MnF_2 nanorods can be attributed to the nanorod structure with small diameter and efficient one-dimensional electron transport pathways. Long cycle performance for 2000 cycles at 10 C with a stabilized capacity of about 430 mAh g^{-1} after activation is also achieved. Furthermore, HRTEM analysis is involved for lithiated and delithiated MnF_2 anodes to elucidate the conversion mechanism for the electrochemical reaction of MnF_2 nanorods with Li at a microscopic level.

Introduction

Over the past few decades, lithium ion battery (LIB) based on new chemistries has been investigated without exhausting its wonders and challenges.[1, 2] Since traditional carbonaceous anode material in commercial LIBs, graphite, has a limited theoretical capacity of 372 mAh g^{-1} together with safety concerns, alternative candidates such as $Li_4Ti_5O_{12}$ and silicon-based alloy/de-alloy type anodes have received intensive exploration.[3, 4] Recently, materials reacting through conversion mechanism have shed light on new anode materials for LIBs by uptaking more than one Li^+ upon discharging with higher theoretical capacities.[5-9] Unlike those extensively studied transition metal oxides such as Co_3O_4, Fe_2O_3, etc, metal fluorides have not been paid much attention until recent years but with promising potential to be explored.[10-12] For instance, considerable interest has been paid for a typical iron-based fluoride FeF_3 as a new cathode with high performance and enhanced safety.[13-15]

MnF_2 can be used as anode material for LIBs with a theoretical specific capacity of 577 mAh g^{-1} (2e- transfer). Although Fu reported the electrochemical performance of MnF_2 thin film fabricated by pulsed laser deposition in the early 2010s,[16] it is not until recently that the superior cycling performance over thousands of cycles of MnF_2 anode has been revealed as well as its capacity activation mechanism.[17] However, apart from initial coulombic inefficiency resulting from conversion reaction, MnF_2 suffers from several major drawbacks shared by metal fluorides which have hindered their achievements of satisfactory electrochemical performance. For instance, poor electronic conductivity due to the large bandgap and high ionicity of metal-fluoride bond remains a problem to be tackled.[18, 19] To address this issue, modification treatments involving efficient conductive wiring (e.g., acetylene black, carbon nanotubes) have been reported to compensate for the intrinsically poor conductivity.[20] Yet, the amount of carbon coating should be carefully controlled because of the negative effects on the powder density, which is estimated to be reduced by a factor of 2 even if only 2 wt% of carbon is present in this composite electrode.[21]

On the other hand, nanostructuring has been opening breathtaking opportunities for improving Li insertion/extraction kinetics owing to the shortened Li^+ solid diffusion pathway in nanomaterials.[22-24] Through shrinking grain size and tailoring various architectures of microstructure for electrodes, enlarged contact area with the electrolyte, increased surface reactivity combined with facile strain relaxation upon electrochemical cycling have led to improved

[a] CAS Key Laboratory of Materials for Energy Conversion, Shanghai Institute of Ceramics, Chinese Academy of Sciences, Shanghai 200050, China. Email: zywen@mail.sic.ac.cn

†Electronic Supplementary Information (ESI) available. See DOI: 10.1039/x0xx00000x

electrochemical performance of pure transition metal fluorides.[25, 26] Good examples such as mesoporous nanostructure with one-dimensional tunnel,[27] worm-like mesoporous structure,[28] hierarchical mesoporous with partially hollow structure,[29] open framework type by top-down synthesis,[30] sponge-like porous film,[31] etc. demonstrate the effective functions of ideal nano-morphologies and stable microstructures on electrochemical enhancement.

One-dimensional nanostructures have so far received increasing interest and offered tremendous impact in various fields since the discovery of carbon nanotubes.[32, 33] Coincidently, when investigated as electrodes in LIBs, a series of one-dimensional nanostructured materials evidently show significant improvements in reversible capacities as well as rate and cycling performance, compared to corresponding bulk materials, which is generally expected due to better capability to withstand stress arising from improved electrical connectivity as well as large structural change arising from large structural change upon cycling.[34, 35] For example, various electrode materials have benefited from the nanorod morphology, such as alpha-Fe_2O_3 nanorods by electrospinning,[36] MoO_2 nanorods by using SBA-15 as hard template, [37] LiV_3O_8 via thermal co-decomposition method[38] and so forth, whose improvements in electrochemistry are usually attributed to the short Li^+ diffusion pathway in radial direction together with the piled porous structure providing fast Li^+ diffusion channels. In particular, nanorod, as one of typical one-dimensional morphologies, shall provide a defined nanostructure to perform mechanism studies at a more microscopic level and help better understand challenges facing MnF_2 anode suffers considerable structural transformation during the conversion reaction.[39, 40]

Herein, we report on the successful discovery of a one-dimensional nanorod structured manganese fluoride anode for the first time via a facile and green solvothermal method. The environmentally friendly and operationally safe fluorine sources ionic liquid ($BmimBF_4$) is employed, instead of the toxic and harmful HF which is usually used in the conventional wet chemistry process. Apart from its unique physical–chemical properties, such as negligible vapor pressure, low viscosity and high thermal stability, the ionic liquid serves not only as the necessary fluorine source but also a soft template for nanostructure control.[41] According to structure and morphology characterization by XRD, SEM and TEM, the as-prepared MnF_2 of pure tetragonal phase displays nanorod-like morphology with a diameter of about 20 nm and length of several hundred nanometers. It is also revealed that the growth of MnF_2 nanorods occurred with a preferred orientation and elongated along [001]. Electrochemical performance of MnF_2 nanorods as anode for rechargeable lithium batteries has been investigated. A low discharge plateau around 0.7 V at 0.1 C of the first cycle is obtained for lithium uptake reaction with a reversible discharge capacity as high as 443 mAh g^{-1}. Enhanced cycling stability for 100 cycles can be observed at various rates with obviously accelerated activation process, indicating shorter time required for complete activation and empowering the MnF_2 anode compared to our previous report. The striking enhancement in the electrochemical Li storage performance in ultrafine MnF_2 nanorods can be attributed to the nanorod structure with small diameter and efficient one-dimensional electron transport pathways. Long cycle performance for 2000 cycles at 10 C with a stabilized capacity of about 430 mAh g^{-1} after activation is also achieved. In addition, ex-situ HRTEM analysis is further performed on lithiated and delithiated MnF_2 electrodes at particular cycled states to reveal the conversion mechanism for the reversible electrochemical reaction of MnF_2 nanorods with Li.

Experimental

Material preparation

Nanorod structured manganese fluoride (MnF_2) was synthesized using $BmimBF_4$ ionic liquid (Shanghai Cheng Jie Chemical Co. Ltd, 99%) as fluorine source and $MnCl_2{\cdot}4H_2O$ (Alfa Aesar, 99%) as manganese source through a solvothermal method. In a typical procedure, metal precursor chloride salts (0.5g) was firstly dissolved in ethanol solvent (30 mL) under stirring at room temperature to form a clear solution. Then, a certain amount of $BmimBF_4$ was added dropwise to the solution followed by vigorous stirring for 1 h. The mixture was further transferred to a Teflon-lined stainless steel autoclave, sealed and heated to 100 ºC and maintained at this temperature for 24 h. The products were washed with acetone and ethanol and centrifuged at 10000 rpm five times to remove residual ionic liquid and other impurities, followed by subsequent drying under 65 ºC for 24h. For comparison, the control samples were also prepared by using same reactants under different solvothermal conditions.

Material characterization

X-Ray powder diffraction (Rigaku Ultima IV, 40 KV/30 mA, Cu-K_α radiation) was used to characterize the phases of the as-prepared materials. The morphology of the as-prepared materials were investigated by a field-emission scanning electron microscopy (FESEM, Magellan 400, FEI) and transmission electron microscopy (TEM, H-800, Hitachi). High-resolution transmission electron microscopy (HRTEM) and selected-area electron diffraction (SAED) measurements were also performed using a JEM-2100F transmission electron microscope.

Electrochemical measurements

The electrochemical characterization for MnF_2 nanorod anode in lithium ion batteries was carried out in coin type cells with lithium foil as both counter and reference electrodes. The working electrodes were prepared by mixing 60 wt% fluorides, 20 wt% acetylene black and 20 wt% poly(vinyldifluoride) (PVDF) dissolved in n-methyl pyrrolidinone (NMP). The slurry was then pasted onto a copper foil substrate followed by drying in vacuum at 80 ºC for 24 h. The average mass loading of the active material MnF2 on each electrode was about 1.5 mg. 1 M $LiPF_6$ in a nonaqueous mixture of ethylene carbonate (EC) and

dimethyl carbonate (DMC) with a volume ratio of 1:1 was employed as electrolyte. Test cells were assembled in an argon-filled glove box with oxygen and water contents less than 1 ppm using Glass fiber (GF/A) from Whatman as separator. Galvanostatic charge-discharge measurements of fluoride anodes vs Li/Li^+ were performed at room temperature under different rates (0.1 to 10 C) in a voltage range of 0.01-3.0 V on a LANDCT2001A battery test system. Cyclic voltammogram measurements were carried out in the same voltage range of 0.01-3.0 V at a scan rate of 0.2 mV/s on an electrochemical workstation (CHI700C). The AC impedance spectrum was measured using Autolab Electrochemical Workstation in a frequency range of 0.1-10^6 Hz. For *ex-situ* HRTEM at different reactive potentials, the cycled electrode sheets were required to be removed from the disassembled batteries and washed with DMC.

Results and discussion

Structure and Morphology Characterization

The crystalline structure of the as-prepared manganese-based fluoride MnF_2 was characterized by X-ray diffraction (XRD) as shown in **Fig. 1**. A series of sharp and strong diffraction peaks assigned to (110), (101), (200), (111), (210), (211), (220), (002), (310), (112), (301) planes are in accordance with those established by JCPDS card No. 80-0926. No peaks of MnF_3 or manganese oxides are observed, indicating successful preparation of pure-phase MnF_2 with tetragonal symmetry (P42/mnm space group).

The microscopic morphology of the as-prepared pure phase MnF_2 was further characterized by field-emission scanning electron microscopy (FESEM) and transmission electron microscopy (TEM) as shown in **Fig. 2**. The FESEM image in Fig. 2a suggests that the synthesized MnF_2 displays a nanorod-like morphology, with a diameter of about 20 nm and length of several hundred nanometers, which is in agreement with the TEM result in Fig. 2d. Such a small diameter can be expected to provide a short transfer path for Li diffusion during insertion and extraction. Particularly, for a typical MnF_2 nanorod presented in Fig. 2b, its single-crystalline structure can be clearly revealed according to the selected-area electron diffraction (SAED) pattern indexed to corresponding planes in Fig. 2c. Meanwhile, as is also shown in the high resolution TEM (HRTEM) image of Fig. 2e and 2f, The distances between well-resolved lattice fringes, 3.30 and 3.45 Å, can be assigned to (001) and (110) of the tetragonal MnF_2 phase, respectively, indicating the growth of MnF_2 nanorods occurred with a preferred orientation and elongated along [001]. Typical unit cell of tetragonal MnF_2 via edge-sharing MnF_6 octahedrons along [001] is shown in Fig. S1.

To further reveal the formation process of MnF_2 nanorods, a series of control experiments with different solvothermal conditions have been carried out. On one hand, influence of reaction time on the nanorod growth was firstly explored as shown in **Fig. 3**(a-c). The samples that were prepared at 100 ºC for different reaction time exhibited a similar nanorod morphology to that of the sample prepared at 100 ºC for 24 h. With the extension of reaction time, stable morphology of nanorod can be preserved with a certain increase of both diameter and length. However, when it comes to elevated temperatures of 120 ºC and 150 ºC, a portion of nanorods

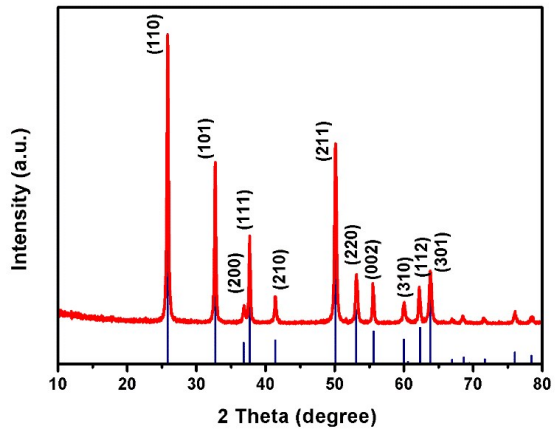

Fig. 1 XRD pattern of the as-prepared manganese-based fluoride MnF_2.

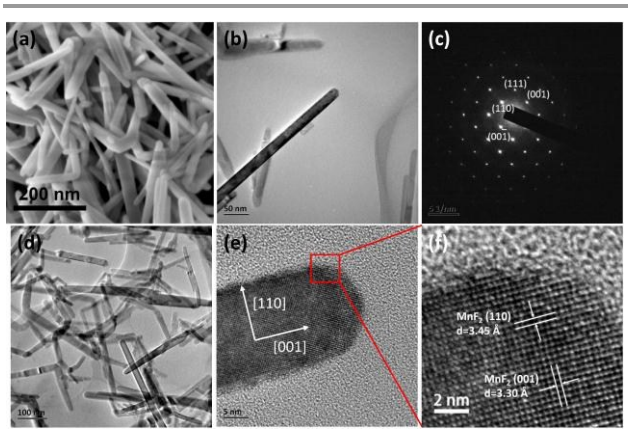

Fig. 2 Typical (a) SEM and (b, d) TEM images of the as-prepared manganese-based fluoride MnF_2 nanorods; (c) Corresponding SAED pattern of (b); (e, f) HRTEM image of the MnF_2 nanorod.

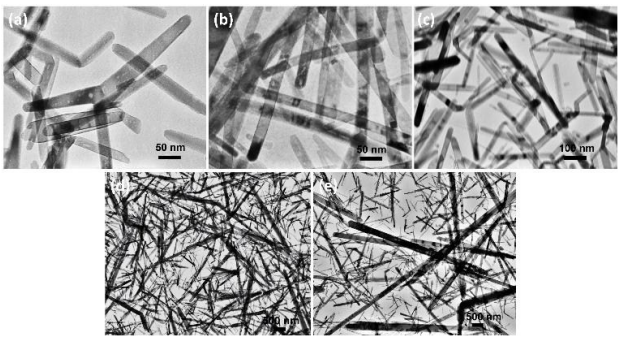

Fig. 3 (a-c) TEM images of the samples that were prepared at 100 ºC for different solvothermal reaction time: (a) 12h; (b) 18h; (c) 30h. (d-e) TEM images of the samples that were prepared for 24h at different solvothermal temperatures: (d) 120 ºC; (d) 150 ºC.

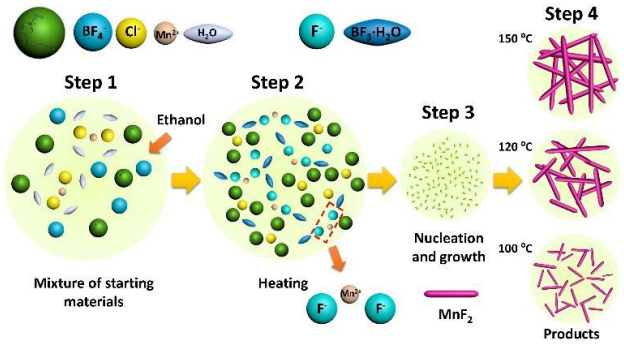

Scheme 1 Proposed formation mechanism of MnF_2 nanorods including Step 1: the mixture of starting materials; Step 2: heating of the reactants; Step 3: nucleation and growth of MnF_2 particles; Step 4: formation of MnF_2 nanorods.

underwent abrupt growth with a sharp increase of diameter to several hundred nanometers and length to even micron scale, leading to inhomogeneous morphology.

In addition, the XRD patterns (ESI, Fig. S2†) demonstrated tetragonal phase of the as-prepared manganese fluoride can be retained but with a remarkable increase of relative peak intensity corresponding to (110) with increasing reaction temperature, also in good agreement with orientation growth of one-dimensional structure shown by previous TEM results. Therefore, the solvothermal reaction condition of 24h at 100 ºC was determined as the most optimal one for homogeneous nanorod-like MnF_2 with favorable yields.

A possible synthesis mechanism of MnF_2 nanorods has been illustrated in **Scheme 1**. When manganese source and ionic liquid are dissolved in ethanol to form corresponding ions, the hydration water separated from the starting material will bring about the hydrolysis of BF_4^-. In this way, F^- can be slowly released under heating conditions as the following formula indicates. [42-44]

$$BF_4^-(IL) + H_2O \rightarrow BF_3 \cdot H_2O(IL) + F^-(IL) \quad (1)$$

Consequently, F^- can be combined with solvated Mn^{2+} to form MnF_2 nuclei. The newly formed nuclei gradually grow with a preferred orientation to form MnF_2 nanorods under suitable solvothermal conditions, which, to some extent, can be ascribed to the possible structural-directing template role of ionic liquid $BmimBF_4$. In particular, cation group $[Bmim]^+$ (1-butyl-3-methylimidazolium) containing an imidazole ring shall act as a capping agent based on its strong interaction with the (110) facet of MnF_2 (as shown in Fig. S3), which can be attributed to several factors as follows.[45, 46] The first factor makes a point of electrostatic interaction between $[Bmim]^+$ and F carrying negative charge whose atom density is higher on (110) facet (ESI, Fig. S4). The second one is based on the hydrogen-bonding interaction existing in the F (MnF_2 surface)-H-C ($[Bmim]^+$ rings) caused by the H atoms in C2 position of $[Bmim]^+$ rings.[47] Moreover, as shown in Fig. S3, if $[Bmim]^+$ ions vertically adsorbed on the (110) plane, the space between $[Bmim]^+$ ions along [001] direction is duplicate d_{001}-spacing (0.660 nm). Fortunately, in various directions, the $[Bmim]^+$ ions are separated in accordance with the mutual π-stacking distance (0.6-0.7 nm) between the aromatic rings.[48, 49] Consequently, we suggest that $[Bmim]^+$ ions can be allowed to anchor onto (110) plane to form relatively tight coverage layer. Last but not least, large steric hindrance of $[Bmim]^+$ ions also contribute to the inhibition of nuclei agglomeration as well as growth. Thus, it can be deduced that ionic liquid serves not only as the necessary fluoride source but also a soft template for nanostructure control.[50]

Electrochemical Lithium-Storage Performance

The electrochemical performance of the manganese fluoride nanorods as anode for rechargeable lithium ion batteries has been carefully evaluated. The galvanostatic charge-discharge process was performed in a voltage range of 0.01-3.0 V at room temperature. As **Fig. 4**a indicated, a low discharge plateau around 0.7 V at 0.1 C of the first cycle is obtained, delivering an initial discharge capacity of 1055 mAh g^{-1}, which can be attributed to the electrochemical reaction of MnF_2 anode with Li, indicating a typical conversion reaction of the as-prepared anode. In spite of the inevitable capacity loss during the initial discharge-charge process, a reversible discharge capacity as high as 443 mAh g^{-1} after early activation from the 10th cycle can be obtained at 0.1 C in the following cycles, higher than that of 300 mAh g^{-1} in our previous work. Besides, higher discharge voltage plateau of subsequent few cycles as compared to the initial one can be observed due to the polarization, in accordance with the right shift of reduction peak as shown by cyclic voltammograms in Fig. 4b. However,

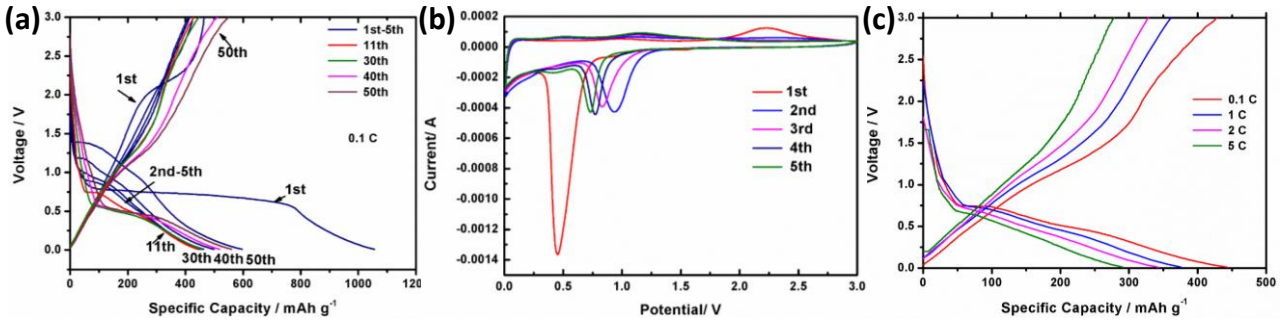

Fig. 4 (a) Discharge-charge curves of MnF_2 anode at 0.1 C between a voltage range of 0.01-3.0 V at typical cycles. (b) Cyclic voltammograms of the first five cycles for the MnF_2 anode between 0.01V and 3.0 V measured at a scan rate of 0.2 mV/s. (c) Discharge-charge curves of the 10th cycle with various rates.

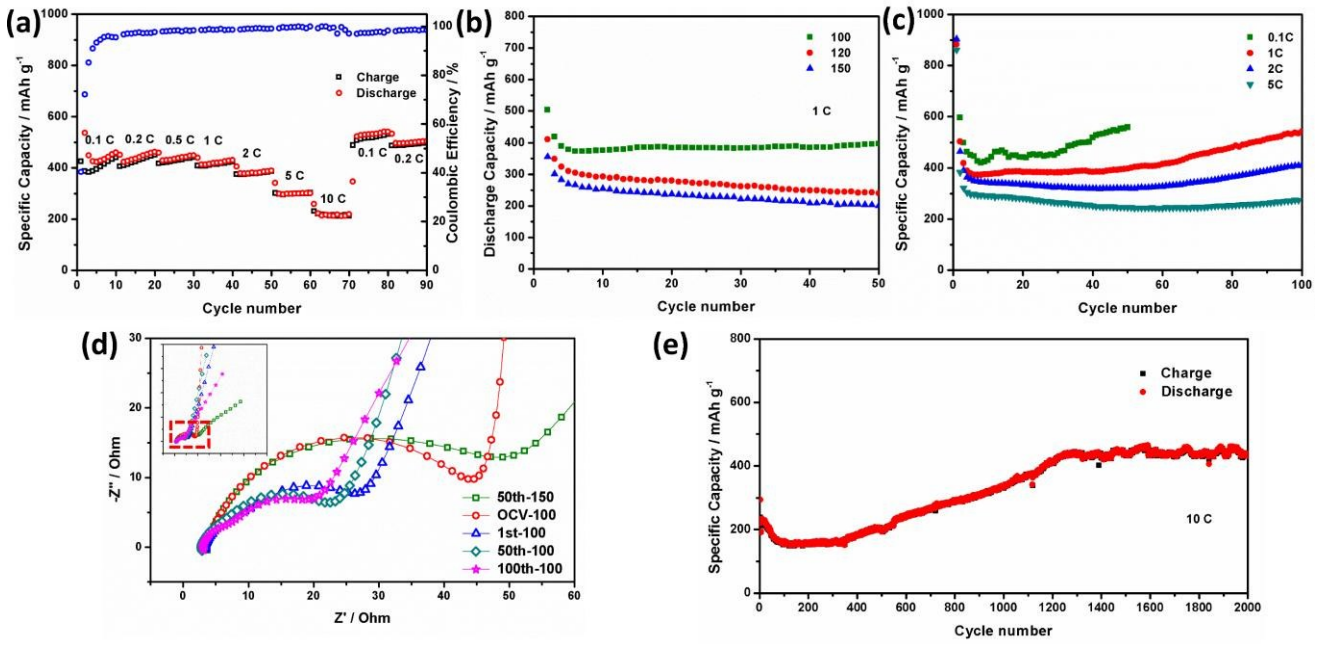

Fig. 5 (a) Rate performance at different rates from 0.1 C to 10 C. (b) Cycle performance plots of the as-prepared MnF_2 nanorod anode together with control samples prepared at different solvothermal temperatures. (c) Discharge capacity as a function of cycle number with various rates. (d) Enlarged view of Nyquist plots of the inset for as-prepared MnF_2 nanorod anode at specified cycles together with the control sample obtained at 150 ºC (e) Long cycle performance with specific capacity as a function of cycle number at 10 C for 2000 cycles.

reduction peaks from the 2nd cycle gradually shifted back towards lower potential which can be evidenced by corresponding stabilization of the discharge-charge curves of the first five cycles in Fig. 4a. The improvement in voltage polarization is believed to be ascribed to enhanced kinetics and reversibility by the early activation concerning improved electrolyte penetration, stabilization of the newly-formed SEI film as well as stress relaxation for the volume change caused by the generation of MnF_2 nanoparticles since the initial conversion process.[19] Moreover, a steady voltage platform around 0.5 V can be maintained since the 30th cycle along with an increase of discharge capacity from 457 mAh g^{-1} in the 30th cycle to 518 mAh g^{-1} in the 40th cycle and further reaching 560 mAh g^{-1} in the 50th cycle. Fig. 4c also presented galvanostatic discharge-charge curves of the as-prepared MnF_2 nanorods of the 10th cycle at various rates from 0.1 C to 5 C after early activation. As can be seen, no evident electrochemical polarization is observed with increasing discharge-charge rates and a large discharge capacity of 291 mAh g^{-1} can still be achieved at a very high rate of 5 C.

Rate performance of the MnF_2 nanorod anode was further examined by first cycling the cell at 0.1 C for ten cycles with a stepwise increase of the discharge/charge rates to 10 C as shown in **Fig. 5**a. Reversible capacities of about 450 mAh g^{-1} at a discharge-charge rate of 0.1 C, 440 mAh g^{-1} at 0.2 C, 430 mAh g^{-1} at 0.5 C, 415 mAh g^{-1} at 1 C, 380 mAh g^{-1} at 2 C, 300 mAh g^{-1} at 5 C and 215 mAh g^{-1} at 10 C are achieved respectively. An outstanding reversibility of the MnF_2 anode was also demonstrated by the overlapping of the discharge and charge capacity in each cycle. Excellent rate performance of the MnF_2 anode indicates both large lithium ion storage and good kinetics due to the fast Li^+ and e^- transportation within the active material resulting from reduced lithium ion pathways of one-dimensional nanostructured fluoride.

Cycle performance of the as-prepared nanorod MnF_2 anode was also performed together with control samples prepared at different solvothermal temperatures to investigate the effect of the morphology and reaction temperature on the electrochemical performance of the MnF_2 anodes. By comparison, cycle performance of the MnF_2 nanorods prepraed at 100 ºC for 50 cycles at 1 C was apparently superior to those prepared at higher temperatures of 120 ºC and 150 ºC. As shown in Fig. 5b, a much higher discharge capacity of 540 mAh g^{-1} (234 mAh g^{-1} for 120 ºC and 187 mAh g^{-1} for 150 ºC) can be observed after 50 cycles without obvious decay from the activated state of 10th cycle, illustrating that electrochemical behavior of MnF_2 anodes can be greatly enhanced by nanorod microstructure with homogeneous morphology and smaller size. To be more specific, the cycling stability of the nanorod MnF_2 anode was further characterized at various discharge-charge rates as presented in Fig. 5c. After 100 cycles, a discharge capacity of 273 mAh g^{-1} at a rather high rate of 5 C can be maintained corresponding to 93.8% of the activated capacity of the 10th cycle. More interestingly, distinct increase trend of capacity can be noticed at 2 C from the 50th cycle, with an increase by 90 mAh g^{-1} after 100 cycles compared to 320 mAh g^{-1} in the 50th cycle. Similar case can also be discovered upon cycling at lower rates in accordance

with the previous phenomenon of capacity increase at 0.1 C in Fig. 4a. Although behaviors of capacity increase have been reported in several metal oxide systems whose reasons are unclear, possible explanations have generally come down to reversible formation and decomposition of organic gel/polymeric like films as well as enhanced reversibility of the conversion reaction itself.[51-54] According to our previous work, a long-term activation process can be found at 10 C for MnF_2 nanocrystals of 100-300 nm with unique self-activation mechanism revealed by ex-situ XPS and HRTEM. Therefore, it is also of importance to discover the noteworthy capacity increase upon cycling at lower rates for MnF_2 with nanorod-like morphology since obviously accelerated activation process indicates shorter time acquired for complete activation and empowering the MnF_2 anode. Herein, AC impedance analysis for the half cell was also carried out before and after electrochemical process at specified cycles at 2 C as plotted in Fig. 5d. An additional semicircle appears in the high frequency region related to the formation of SEI film after initial Li^+ uptaking/extraction process compared to the OCV (Open Circuit Voltage) state.[55]. Besides, smaller interface impedance can be observed in the plots at 50th and 100th cycle corresponding to increased electron and Li^+ diffusion rate, somehow interpreting the capacity increase within 100 cycles discussed previously.[56]. On the contrary, much higher impedance can be noticed for the control sample at 50th cycle whose semicircle related to R_{SEI} no longer exists, further reflecting the importance of the shrinking of size on capability and cyclability. All the fitting results (ESI, Table S1) were obtained by NOVA software with the equivalent circuit (ESI, Fig. S5).

More importantly, long-term cycle performance was further examined by cycling the MnF_2 nanorod anode at 10 C for 2000 cycles as shown in Fig. 5e. Remarkably, a maximum discharge capacity of about 430 mAh g^{-1} at around 1500 cycles resulting from the typical long-term electrochemical activation process of MnF_2 was also revealed, which agreed with the previous report.[17] The stabilized capacity was then maintained to 2000 cycles whose electrochemical activation degree was also improved compared to the maximum value of about 300 mAh g^{-1} in our previous work. Detailed explanation for this long-term activation process can be found in the further discussion section.

Greatly enhanced rate capability of MnF_2 nanorod anode can be further illustrated by comparison with MnF_2 nanocrystalline anode reported by our group previously as shown in **Fig. 6**. Specifically, the discharge capacity of MnF_2 nanorod anode has been increased by ~150 mAh g^{-1} at 0.1 C and an increase of ~100 mAh g^{-1} can be achieved at a high current density of 5 C. Herein, MnF_2 nanorod anode yields much better rate capability, which can be attributed mainly to the small diameter of nanorod ensuring effectively shortened radial diffusion pathways for both Li^+ and e^- and thus facilitating their fast transfer. Moreover, superior lithium storage of MnF_2 nanorod anode can also be proved by comparison with other transition metal fluorides possessing similar 1D morphology (ESI, Table S2).

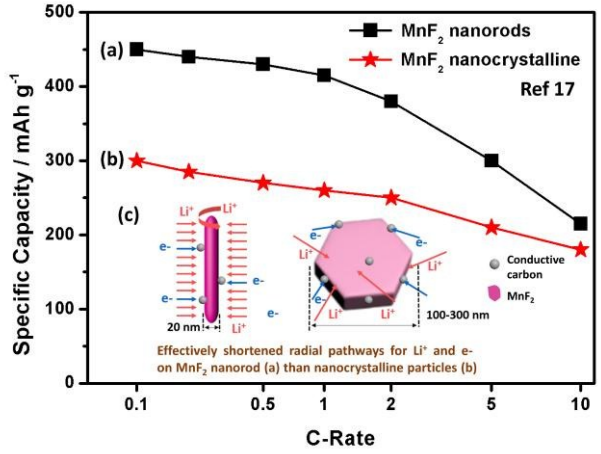

Fig. 6 Comparison of rate capability of (a) MnF_2 nanorod anode with (b) MnF_2 nanocrystalline anode reported previously.

Reaction Mechanism

Ex-situ HRTEM was further performed on cycled electrodes to take a closer check of the evolution of morphology and structure of the MnF_2 nanorod anodes after discharge and

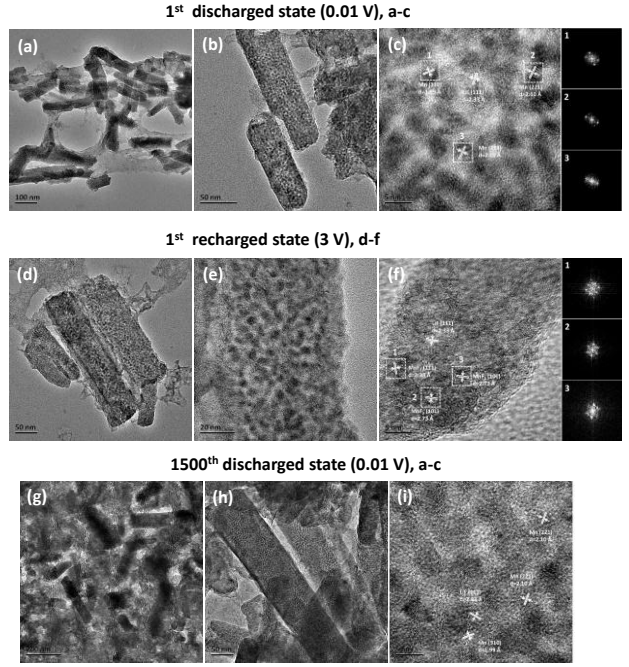

Fig. 7 Microstructural characterization of the MnF_2 nanorod anode after electrochemical reactions. (a, b) Representative TEM images for the MnF_2 nanorod anode at the first discharged (lithiated) state. (c) HRTEM image confirming the generation of LiF matrix and metallic Mn domains with corresponding FFT images. (d, e) Representative TEM images for the MnF_2 nanorod anode at the first recharged (delithiated) state. (f) HRTEM image confirming the regeneration of MnF_2 nanocrystallines with corresponding FFT images and remaining LiF. (g, h) Representative TEM images for the MnF_2 nanorod anode at the 1500th discharged (lithiated) state. (i) HRTEM image confirming the generation of LiF matrix and interconnected metallic Mn domains after long-term activation.

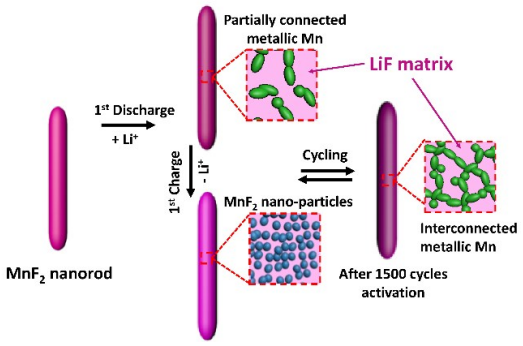

Scheme 2 Schematics of the microstructure and local chemistry changes of the MnF_2 nanorod anode during different electrochemical stages.

charge process. As can be seen from typical TEM images in **Fig. 7**a and 7b, the MnF_2 nanorods embedded in the conducting carbon agent have been electrochemically reduced to two obvious different phases upon discharge to 0.01 V, with small dark domains (5-8 nm) clearly scattering all over the lithiated nanorods. Those nanodomains with dark contrast can be indexed to metallic manganese with corresponding planes of (221) and (310), according to the analyzed HRTEM results in Fig. 7c as well as corresponding fast Fourier Transform (FFT) patterns for selected areas. Moreover, the converted LiF matrix with (111) plane has also been marked within the bright background since the LiF phase is less visible than the Mn phase due to the weak scattering of light constituent elements. Similar microstructural feature has been previously reported for FeF_3 cathodes with corresponding conversion product of LiF and metallic Fe when discharged to 1.5 V.[57]

When the anode is recharged to 3.0 V, TEM images in Fig. 7d and 7e show that newly created MnF_2 nanoparticles (2-3 nm) have been regenerated from LiF and Mn within the nanorods, which is consistent with previous reports for typical conversion reaction electrodes. Several merits benefiting from those uniformly dispersed nanodomains such as reduced particle size of active material and higher reactivity for electrochemistry shall ensure great electrochemical performance of MnF_2 anode. HRTEM image in Fig. 7e also displayed well-defined lattice fringes of MnF_2 (101) and (111) with corresponding FFT patterns (Fig. 7f), confirming the nanocrystalline nature of the recharged nanorods. Besides, certain amount of LiF without complete decomposition can still be detected in the bright background, indicating the incomplete reversibility of the conversion reaction. In brief, the MnF_2 nanorod anode undergoes a typical conversion reaction with inevitable capacity loss during the initial discharge/charge process through the following reaction scheme:

$$MnF_2 + 2Li^+ + 2e^- \rightarrow Mn(nano)/LiF \text{ (Discharge)} \quad (2)$$

$$Mn(nano) + LiF - 2Li^+ \rightarrow MnF_2(nano) + 2e^- \text{(Charge)} \quad (3)$$

Further investigation on the phase and microstructure of the MnF_2 nanorod anode was set out after 1500 cycles at the long-term electrochemical activated state as shown in **Fig. 7**g-i. At the discharged state to 0.01 V of the 1500th cycle, much smaller size of Mn (2-3 nm) than the one at 1st discharged state can be observed, which are interconnected from one with each other to form continuous network within the LiF matrix on a microscopic level. Successful regeneration of metallic Mn was also confirmed by HRTEM results in Fig. 7i. According to our previous report with detailed explanation for the long-term activation phenomenon, similar transformation of local structure and phase distribution was also observed herein, leading to the greatly enhanced electrochemical reversibility which can be attributed to the continuous network of Mn facilitating local electron transport in short. To illustrate, the long-term activation process has been summarized by a schematic illustration of the MnF_2 nanorod anode during different electrochemical stages all over the 2000 cycles as shown in **Scheme 2**. With regard to inevitable issues such as pulverization of anode as well as decomposition of electrolyte and deterioration of the Li electrode during the long-term electrochemical process, future work should focus on strategies such as effectively conductive coating on nanorods so that volume strain could be effectively buffered and accommodated for a better capacity retention.[58, 59]

Conclusions

In summary, we report on the successful discovery of a one-dimensional nanorod structured Manganese Fluoride anode for the first time via a facile and green solvothermal method with ionic liquid ($BmimBF_4$) as the fluorine source. The as-prepared MnF_2 of pure tetragonal phase displays nanorod-like morphology with a diameter of about 20 nm and length of several hundred nanometers. It is also revealed that the growth of MnF_2 nanorods occurred with a preferred orientation and elongated along [001]. Electrochemical performance of MnF_2 nanorods as anode for rechargeable lithium batteries is investigated. A low discharge plateau around 0.7 V at 0.1 C of the first cycle is obtained for lithium uptake reactions with a reversible discharge capacity as high as 443 mAh g^{-1}. Enhanced cycling stability for 100 cycles can be observed at various rates with obviously accelerated activation process, indicating shorter time required for complete activation and empowering the MnF_2 anode. The striking enhancement in the electrochemical Li storage performance in ultrafine MnF_2 nanorods such as better rate capability can be attributed to the nanorod structure with small diameter and efficient one-dimensional electron transport pathways. Long cycle performance for 2000 cycles at 10 C with a stabilized capacity of about 430 mAh g^{-1} after activation is also achieved, indicating the application of MnF_2 nanorods as promising anode material for future lithium batteries with long cycle life. In addition, typical conversion mechanism is revealed by further performing ex-situ HRTEM analysis on lithiated and delithiated MnF_2 electrodes at particular cycled states, along with the confirmation of continuous network of metallic Mn responsible for the improved reversible electrochemical reaction of MnF_2 nanorods with Li. According to these important findings, new opportunities could be opened up in constructing high performance lithium ion batteries with

superior conversion MnF_2 anode for energy storage and other critical applications.

Acknowledgements

This work was supported by the National Natural Science Foundation of China (No. 51432010) and Key Fundamental Research Project from Science and Technology Commission of Shanghai Municipality (14JC1493000).

Notes and references

1. M. R. Palacin, *Chem Soc Rev*, 2009, **38**, 2565-2575.
2. R. Marom, S. F. Amalraj, N. Leifer, D. Jacob and D. Aurbach, *J. Mater. Chem.*, 2011, **21**, 9938-9954.
3. H. K. Liu, Z. P. Guo, J. Z. Wang and K. Konstantinov, *J. Mater. Chem.*, 2010, **20**, 10055-10057.
4. W.-J. Zhang, *J. Power Sources*, 2011, **196**, 13-24.
5. R. Malini, U. Uma, T. Sheela, M. Ganesan and N. G. Renganathan, *Ionics*, 2009, **15**, 301-307.
6. J. Cabana, L. Monconduit, D. Larcher and M. Rosa Palacin, *Adv. Mater.*, 2010, **22**, E170-E192.
7. M. V. Reddy, G. V. S. Rao and B. V. R. Chowdari, *Chem. Rev.*, 2013, **113**, 5364-5457.
8. Y. Guo, L. Yu, C.-Y. Wang, Z. Lin and X. W. D. Lou, *Adv. Funct. Mater.*, 2015, **25**, 5184-5189.
9. H. B. Wu, J. S. Chen, H. H. Hng and X. W. Lou, *Nanoscale*, 2012, **4**, 2526-2542.
10. M. V. Reddy, T. Yu, C. H. Sow, Z. X. Shen, C. T. Lim, G. V. S. Rao and B. V. R. Chowdari, *Adv. Funct. Mater.*, 2007, **17**, 2792-2799.
11. Y. F. Zhukovskii, E. A. Kotomin, P. Balaya and J. Maier, *Solid State Sci.*, 2008, **10**, 491-495.
12. M. V. Reddy, G. Prithvi, K. P. Loh and B. V. R. Chowdari, *ACS Appl. Mater. Interfaces*, 2014, **6**, 680-690.
13. S. Kim, D. Seo, H. Gwon, J. Kim and K. Kang, *Adv. Mater.*, 2010, **22**, 5260-5264.
14. R. F. Li, S. Q. Wu, Y. Yang and Z. Z. Zhu, *J. Phys. Chem. C*, 2010, **114**, 16813-16817.
15. T. Li, L. Li, Y. L. Cao, X. P. Ai and H. X. Yang, *J. Phys. Chem. C*, 2010, **114**, 3190-3195.
16. Y. Cui, M. Xue, K. Hu, D. Li and Z. Fu, *J. Inorg. Mater.*, 2010, **25**, 145-150.
17. K. Rui, Z. Wen, Y. Lu, J. Jin and C. Shen, *Adv. Energy Mater.*, 2014, DOI: 10.1002/aenm.201401716.
18. H. Li, G. Richter and J. Maier, *Adv. Mater.*, 2003, **15**, 736-739.
19. H. Li, P. Balaya and J. Maier, *J. Electrochem. Soc.*, 2004, **151**, A1878-A1885.
20. F. Badway, F. Cosandey, N. Pereira and G. G. Amatucci, *J. Electrochem. Soc.*, 2003, **150**, A1318-A1327.
21. C. Delacourt, P. Poizot, S. Levasseur and C. Masquelier, *Electrochem. Solid State Lett.*, 2006, **9**, A352-A355.
22. A. S. Arico, P. Bruce, B. Scrosati, J. M. Tarascon and W. Van Schalkwijk, *Nat. Mater.*, 2005, **4**, 366-377.
23. P. G. Bruce, B. Scrosati and J. M. Tarascon, *Angew. Chem. Int. Ed. Engl.*, 2008, **47**, 2930-2946.
24. S. A. Corr, in *Nanoscience: Volume 1: Nanostructures through Chemistry*, The Royal Society of Chemistry, UK, 2013, vol. 1, pp. 180-207.
25. Z. W. Fu, C. L. Li, W. Y. Liu, J. Ma, Y. Wang and Q. Z. Qin, *J. Electrochem. Soc.*, 2005, **152**, E50-E55.
26. H. Zhang, Y. Zhou, Q. Sun and Z. Fu, *Solid State Sci.*, 2008, **10**, 1166-1172.
27. C. L. Li, L. Gu, J. W. Tong, S. Tsukimoto and J. Maier, *Adv. Funct. Mater.*, 2011, **21**, 1391-1397.
28. Y. Lu, Z. Wen, K. Rui, X. Wu and Y. Cui, *J. Power Sources*, 2013, **244**, 306-311.
29. Y. Lu, Z. Wen, J. Jin, K. Rui and X. Wu, *Phys. Chem. Chem. Phys.*, 2014, **16**, 8556-8562.
30. C. Li, C. Yin, X. Mu and J. Maier, *Chem. Mater.*, 2013, **25**, 962-969.
31. M. Jin, G. Zhang, F. Yu, W. Li, W. Lu and H. Huang, *Phys. Chem. Chem. Phys.*, 2013, **15**, 1601-1605.
32. S. A. Corr, M. Grossman, Y. F. Shi, K. R. Heier, G. D. Stucky and R. Seshadri, *J. Mater. Chem.*, 2009, **19**, 4362-4367.
33. H. B. Wu, G. Zhang, L. Yu and X. W. Lou, *Nanoscale Horiz.*, 2016, DOI: 10.1039/c5nh00023h.
34. J. R. Szczech and S. Jin, *Energy Environ. Sci.*, 2011, **4**, 56-72.
35. C. K. Chan, X. F. Zhang and Y. Cui, *Nano Lett.*, 2008, **8**, 307-309.
36. C. T. Cherian, J. Sundaramurthy, M. Kalaivani, P. Ragupathy, P. S. Kumar, V. Thavasi, M. V. Reddy, C. H. Sow, S. G. Mhaisalkar, S. Ramakrishna and B. V. R. Chowdari, *J. Mater. Chem.*, 2012, **22**, 12198-12204.
37. B. Guo, X. Fang, B. Li, Y. Shi, C. Ouyang, Y.-S. Hu, Z. Wang, G. D. Stucky and L. Chen, *Chem. Mater.*, 2012, **24**, 457-463.
38. A. Pan, J. Liu, J.-G. Zhang, G. Cao, W. Xu, Z. Nie, X. Jie, D. Choi, B. W. Arey, C. Wang and S. Liang, *J. Mater. Chem.*, 2011, **21**, 1153-1161.
39. X. H. Liu and J. Y. Huang, *Energy Environ. Sci.*, 2011, **4**, 3844-3860.
40. W. H. Shin, T. H. Hwang, Y. S. Huh and J. W. Choi, *J. Electrochem. Soc.*, 2012, **159**, A2143-A2147.
41. D. S. Jacob, L. Bitton, J. Grinblat, I. Felner, Y. Koltypin and A. Gedanken, *Chem. Mater.*, 2006, **18**, 3162-3168.
42. Gillespi.Rj and J. S. Hartman, *Can. J. Chem.*, 1967, **45**, 2243-2246.
43. C. Zhang, J. Chen, Y. C. Zhou and D. Q. Li, *J. Phys. Chem. C*, 2008, **112**, 10083-10088.
44. L. Zhu, Q. Li, X. D. Liu, J. Y. Li, Y. F. Zhang, J. Meng and X. Q. Cao, *J. Phys. Chem. C*, 2007, **111**, 5898-5903.
45. W. J. Zheng, X. D. Liu, Z. Y. Yan and L. J. Zhu, *Acs Nano*, 2009, **3**, 115-122.
46. H. Kaper, F. Endres, I. Djerdj, M. Antonietti, B. M. Smarsly, J. Maier and Y. S. Hu, *Small*, 2007, **3**, 1753-1763.
47. K. Dong, S. Zhang, D. Wang and X. Yao, *J. Phys. Chem. A*, 2006, **110**, 9775-9782.
48. O. M. Yaghi, G. Li and H. Li, *Nature*, 1995, **378**, 703-706.
49. J. Jin, T. Iyoda, C. Cao, Y. Song, L. Jiang, T. J. Li and D. B. Zhu, *Angew. Chem.*, 2001, **113**, 2193-2196.
50. Z. J. Miao, Z. M. Liu, K. L. Ding, B. X. Han, S. D. Miao and G. M. An, *Nanotechnology*, 2007, **18**, 125605-125609.
51. P. Poizot, S. Laruelle, S. Grugeon, L. Dupont and J. M. Tarascon, *Nature*, 2000, **407**, 496-499.
52. L. Taberna, S. Mitra, P. Poizot, P. Simon and J. M. Tarascon, *Nat. Mater.*, 2006, **5**, 567-573.
53. J. Jamnik and J. Maier, *Phys. Chem. Chem. Phys.*, 2003, **5**, 5215-5220.
54. S. Laruelle, S. Grugeon, P. Poizot, M. Dolle, L. Dupont and J. M. Tarascon, *J. Electrochem. Soc.*, 2002, **149**, A627-A634.

55. S. Yang, X. Feng and K. Mullen, *Adv. Mater.*, 2011, **23**, 3575-3579.
56. M. D. Levi, G. Salitra, B. Markovsky, H. Teller, D. Aurbach, U. Heider and L. Heider, *J. Electrochem. Soc.*, 1999, **146**, 1279-1289.
57. L. Li, F. Meng and S. Jin, *Nano Lett.*, 2012, **12**, 6030-6037.
58. C. Wang, L. Yin, D. Xiang and Y. Qi, *ACS Appl. Mater. Interfaces*, 2012, **4**, 1636-1642.
59. D. N. Wang, J. L. Yang, X. F. Li, D. S. Geng, R. Y. Li, M. Cai, T. K. Sham and X. L. Sun, *Energy Environ. Sci.*, 2013, **6**, 2900-2906.